A Biocompatible Vibration-Actuated Omni-Droplets Rectifier with Large Volume Range Fabricated by Femtosecond Laser

Yiyuan Zhang, Jing Li, Le Xiang, Jinxing Wang, Tao Wu, Yunlong Jiao, Shaojun Jiang, Chuanzong Li, Shengying Fan, Juan Zhang, Hao Wu, Yuxuan Zhang, Yucheng Bian, Kun Zhao, Yubin Peng, Wulin Zhu, Jiawen Li, Yanlei Hu, Dong Wu,* Jiaru Chu, and Zuankai Wang*

High-performance droplet transport is crucial for diverse applications including biomedical detection, chemical micro-reaction, and droplet microfluidics. Despite extensive progress, traditional passive and active strategies are restricted to limited liquid types, small droplet volume ranges, and poor biocompatibilities. Moreover, more challenges occur for biological fluids due to large viscosity and low surface tension. Here, a vibration-actuated omni-droplets rectifier (VAODR) consisting of slippery ratchet arrays fabricated by femtosecond laser and vibration platforms is reported. Through the relative competition between the asymmetric adhesive resistance originating from the lubricant meniscus on the VAODR and the periodic inertial driving force originating from isotropic vibration, the fast (up to ≈60 mm s^{-1}), programmable, and robust transport of droplets is achieved for a large volume range (0.05–2000 µL, $V_{max}/V_{min} \approx 40 000$) and in various transport modes including transport of liquid slugs in tubes, programmable and sequential transport, and bidirectional transport. This VAODR is general to a high diversity of biological and medical fluids, and thus can be used for biomedical detection including ABO blood-group tests and anticancer drugs screening. These strategies provide a complementary and promising platform for maneuvering omni-droplets that are fundamental to biomedical applications and other high-throughput omni-droplet operation fields.

1. Introduction

Intelligent droplet transport on interfaces plays an important role in numerous applications such as biomedical detection,[1–3] chemical microreaction,[4–6] and droplet microfluidics.[7–10] Previous droplet transport strategies can be typically classified into two categories: passive control[11–20] without external energy input and active manners with external energy input.[21–35] Passive strategies include sole surface chemical gradient,[11] topographical gradient (e.g., "V-shaped"),[12–15] and conical structure[16–18] or tubes.[19,20] For instance, Chaudhury and Whitesides[11] reported a typical droplet motion on the tilted solid substrate originating from the imbalance of the surface tension forces acting on the droplet edges induced by surface chemical gradient. Prakash et al.[15] discovered that the shorebird could move droplets from the tip of beak to its mouth in a stepwise ratcheting fashion by repeatedly opening and closing their beak to form a

Y. Zhang, J. Wang, S. Jiang, H. Wu, Y. Zhang, Y. Bian, Y. Peng, W. Zhu, J. Li, Y. Hu, D. Wu, J. Chu
CAS Key Laboratory of Mechanical Behavior and Design of Materials
Key Laboratory of Precision Scientific Instrumentation of Anhui Higher Education Institutes
Department of Precision Machinery and Precision Instrumentation
University of Science and Technology of China
Hefei 230027, China
E-mail: dongwu@ustc.edu.cn
J. Li, Z. Wang
Department of Mechanical Engineering
City University of Hong Kong
Hong Kong, China
E-mail: zuanwang@cityu.edu.hk

L. Xiang, C. Li
School of Instrument Science and Opto-electronics Engineering
Hefei University of Technology
Hefei 230009, P. R. China
T. Wu
Department of Modern Mechanics
University of Science and Technology of China
Hefei 230027, China
Y. Jiao
Institute of Tribology
Hefei University of Technology
Hefei 230009, P. R. China
S. Fan
Center for Biomedical Engineering
Department of Electronic Science and Technology
University of Science and Technology of China
Hefei 230026, China

**ADVANCED
SCIENCE NEWS**

www.advancedsciencenews.com

**ADVANCED
MATERIALS**

www.advmat.de

"V"-shaped topography. Zheng et al.[16] showed that the water-collecting ability of the capture silk of the spider is attributed to the unique conical structures. Li et al.[19] demonstrated the utility of peristome-mimetic tubular structures for water elevation by bending biomimetic plates into tubes. However, these strategies have severe inherent limitations including short transport distance, slow transport velocity, and limited volume range, which greatly hinder their practical applications.

To achieve a controllable on-demand transport of droplets, active strategies with external energy input including electric (e.g., electrowetting),[21–24] magnetic (e.g., magnetic droplet or magnetic microtextures),[25–28] light (e.g., light–heat transformation, light-induced surface modification, light-induced deformable polymers),[29–31] and thermal (e.g., evaporation gradient and Leidenfrost effect)[32–35] fields have been extensively reported. For example, Li et al.[21] demonstrated a method to manipulate droplets by using electrical signals to induce the liquid to dewet, rather than wet, a hydrophilic conductive substrate without added layers with a low driving voltage and current. Especially, Sun et al.[24] reported a high-velocity and long-range transport of droplets elicited by novel surface charge-density gradients on diverse substrates. Wang et al.[26] introduced a hierarchical magnetoresponsive composite surface by infiltrating a ferrofluid into a microstructured matrix for the manipulation and transport of droplets. Lv et al.[30] presented a strategy to manipulate liquid slugs by photoinduced asymmetric deformation of tubular microactuators induced by capillary forces. Quéré et al.[35] achieved and elucidated a droplet propulsion on a hot ratchet in a well-defined direction at a definite velocity. Nonetheless, there are some critical defects among these methods that limit their practical applications. Specifically, electro-wetting or electro-dewetting needs to fabricate numerous electric units on the substrate, and the economic and time cost are relatively high. Magnetic actuation needs doping magnetic particles into droplets or substrates, subsequently introducing contamination for droplet transport. Meanwhile, the substrate must be flexible and deformable which is not applicable to rigid surfaces. Light-induced droplet motion is usually limited by the low locomotion speed and small volume ranges due to the extremely weak capillary driving forces. Besides, thermal and evaporation need a local high temperature to generate a surface tension gradient, which are not applicable to most scenarios that need a normal environment. In general, these methods are not easy to satisfy the up-to-date practical requirements especially in the aspects of biocompatible manipulation of omni-droplets with large volume ranges.

J. Zhang
Department of Clinical Laboratory
The First Affiliated Hospital of USTC
Division of Life Sciences and Medicine
University of Science and Technology of China
Hefei, Anhui 230001, China
K. Zhao
Information Materials and Intelligent Sensing Laboratory of Anhui Province
School of Electronics and Information Engineering
Anhui University
Hefei 230039, China

Compared with other counterparts, mechanical vibration has broad advantages including robustness and durability, and no cross-contamination. Mechanical vibration as a stimulation strategy was first proposed by Daniel et al. to achieve a droplet motion on chemical gradient surfaces.[36–38] Later, Demirel et al.[39] and Bohringer et al.[40] developed different substrate materials combined with mechanical vibration to achieve droplet transport with an enhanced transport capacity. Relying on the superhydrophobic slant microwalls array, our previous work has achieved the unidirectional water-based droplet transport and demonstrated a promising transport capacity.[41] Nevertheless, the reported transport performance is still limited, especially in the core transport capacity (e.g., volume range, transport speed, and liquid types). In addition, due to their extremely complex composition, large viscosity, and low surface tension, the manipulation of biological fluids remains elusive. The slippery liquid-infused porous surfaces inspired by *Nepenthes* pitcher plants could form a stable, defect-free, and inert "slippery" interface to achieve the state-of-the-art liquid-repellent surfaces to repel complex fluids such as hydrocarbons, crude oil, and blood samples.

Here, we report a vibration-actuated omni-droplets rectifier (VAODR) fabricated by femtosecond laser oblique ablation (FLOA) and lubricant-infusion, which enables the large-volume omni-droplet transport in a biocompatible way without the need of doping of characteristic nanoparticles, electrical damage, and heat (high-temperature) damage. By tailoring the conjunction between the anisotropic adhesive resistance force due to the asymmetric slippery ratchets under the actuation of periodic inertial driving force originating from isotropic mechanical horizontal vibration, the large transport volume range (0.05–2000 μL, $V_{max}/V_{min} \approx$ 40 000) and high transport speed ($\approx$60 mm s^{-1}) of droplets can be well maintained, which is three orders of magnitude and three times higher than previous works,[36–40] respectively. Note that a large-volume water droplet ($\approx$2 mL) could also be transported on the VAODR which is by far less known even under the actuation of other external stimulation such as electric, magnetic, light, and thermal field. Such a VAODR can be applied to a large range of liquids including biological and medical fluids (Movies S1 and S2, Supporting Information), cell culture medium, alcohol solution, and liquid metal. Based on this versatile platform, transport of liquid slugs in a VAODR-based tube, programmable and sequential transport with broad volume ranges, real-time switching of sliding/pinning, and "cable-car"-like bidirectional transport have also been demonstrated. The VAODR is applicable to the majority of solid substrates including metals, semiconductors, and polymers. The robustness and durability of the VAODR are also verified to manipulate droplets up to 50 cycles with negligible decrease in speed. Finally, to highlight the potential application of the VAODR, we have conducted a series of biomedical detections, including an ABO blood-group test and anticancer drug screening by designing typical intriguing functional devices including a hand-held detection gun and portable detection kits based on the VAODR. We envision that this conceptional VAODR could benefit the related fields such as high-throughput on-demand interfacial microfluidics management as well as biomedical detection.

2. Results and Discussion

2.1. Unidirectional and Velocity-Controllable Transport of Droplets on VAODR

As shown in **Figure 1**A, our VAODR consists of anisotropic slippery ratchets, which is fabricated by FLOA (oblique angle: α) and infused with lubricant (silicone oil), and horizontal vibration platform. A droplet deposited on the VAODR is propelled directionally along the X-axis under the actuation of horizontal vibrational rectification at a climbing angle on the asymmetric microstructures (slant ratchets) that offer the anisotropy which is essential to unidirectional motion of droplets. The slippery effect of infused lubricant can significantly reduce resistance of droplet transport. The external stimulation, namely, mechanical horizontal vibration can input external energy to actuate the droplet motion. Relying on the conjunction of these three basic elements, a directional ($\approx$5.39 mm s^{-1}) motion of

a water droplet with the volume of $\approx$6 µL on the VAODR at a climbing angle (β) of $\approx$3.5° is realized (Figure 1B). Then, by utilizing scanning electron microscopy (SEM) images, we fully characterize the asymmetric bare ratchets with oblique angle of slant ratchets (γ) $\approx$45°, ratchet depth (D) $\approx$134 µm, groove width (W; full-width at half-maximum) $\approx$174 µm, and structure period (P) $\approx$220 µm (Figure 1C, side and top view) fabricated on the poly(dimethylsiloxane) (PDMS) membrane using the home-made femtosecond laser oblique processing system in Figure S1, Supporting Information. After that, the ratchets are infused with lubricant to render themselves with slipperiness for drag reduction (Experimental Section). The lubricant menisci are tuned preciously and controllably by the amount of infused lubricant utilizing ultrasonic processing or spin coating in Figure 1D and Figures S2 and S3, Supporting Information. For thin oil film ($t/D \approx$17.2%), the lubricant partially covers the ratchets and thus the asymmetry of the VAODR is prominent with little hysteresis. The contact area of droplet with slippery
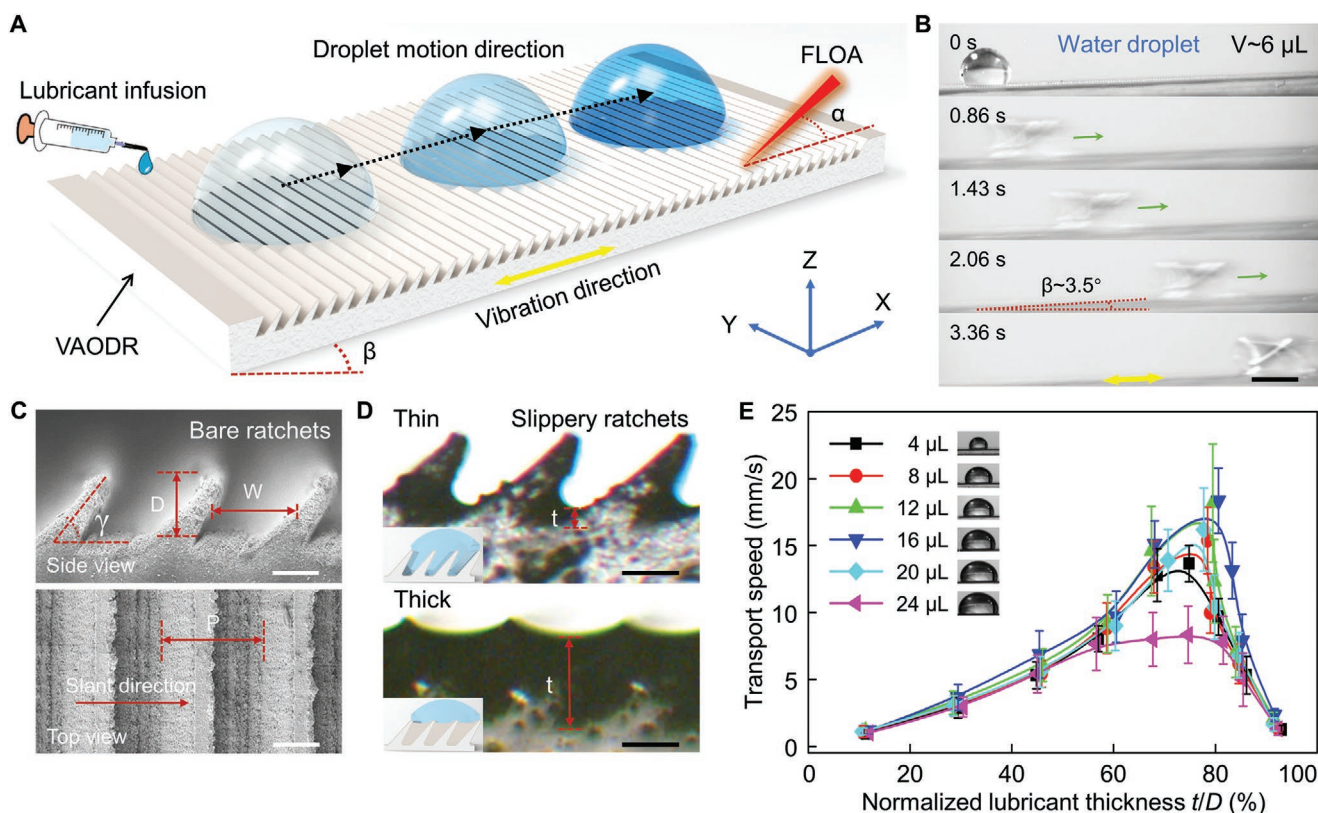

Figure 1. Unidirectional and velocity-controllable transport of droplets on the VAODR. A) Schematic illustration of the process of directional droplet transport mediated by horizontal vibrational rectification at a climbing angle (β) on anisotropic slippery ratchets fabricated by FLOA (oblique angle: α) combined with lubricant infusion. B) Selected sequential snapshots of a water droplet ($\approx$6 µL) transport with a rapid velocity of $\approx$5.39 mm s^{-1} on the slippery ratchets at a climbing angle of $\approx$3.5° actuated by horizontal vibrational. The green unidirectional arrows indicate the direction of the instant droplet velocity and the yellow bidirectional arrow represents the horizontal vibrational. Scale bar: 3 mm. C) Side and top SEM images of anisotropic bare ratchets indicate a ratchet depth (D) of $\approx$134 µm, groove width (W) of $\approx$174 µm, period (P) of $\approx$220 µm (plate width of $\approx$46 µm), and oblique angle (γ) of ratchets of $\approx$45°. These topological parameters could be finely tunable (e.g., D: 0–260 µm, W: 0–150 µm, and P: 0–230 µm). Scale bar: 100 µm. D) Microscopy photographs of slippery ratchets with a thin and thick lubricant (silicone oil) film thickness (t), which affects the anisotropy of the ratchets. Thin lubricant film corresponds to a strong anisotropy but a weak slippery effect, while thick lubricant film corresponds to a weak anisotropy but a strong slippery effect. The insets show the illustrations of droplets deposited on slippery ratchets with two extreme thicknesses. Scale bar: 50 µm. E) There is an optimal lubricant thickness ($t/D \approx$75%) corresponding to the highest transport speed of water droplets with different volumes (4–24 µL), which may balance the texturing of topological anisotropy and the functionalizing of chemical slipperiness. By precisely regulating lubricant thickness (40–100 µm) through changing the ultrasonic processing time, the transport speed of the water droplets with different volumes can be modulated precisely (0–20 mm s^{-1}) for controllable transport.

**ADVANCED
SCIENCE NEWS**

www.advancedsciencenews.com

**ADVANCED
MATERIALS**

www.advmat.de

ratchets is large (inset in top panel). In contrast, for the thick oil film ($t/D \approx 90.2\%$), the lubricant fully covers the asymmetric ratchets and thus the asymmetry of the VAODR is eliminated with great slipperiness, which impair the droplet transport. The contact area of droplet with slippery ratchets is small (inset in bottom panel). So there must be, theoretically, an optimal thickness of lubricant film that balances the anisotropy and slippery effects of the VAODR for an optimal capacity (e.g., maximum transport velocity) of droplet transport. By modulating the lubricant thickness t/D from 10% to 93% utilizing ultrasonic processing in air, different transport velocity (up to $\approx$20 mm s^{-1}) of water droplets with a wide range of volumes varying from 4 to 24 µL can be achieved (Figure 1E).

2.2. High-Speed Dynamic Process and Physical Mechanism of Directional Droplet Transport on VAODR

To propose the mechanics model of droplet transport on the VAODR, we experimentally capture the droplet motion by high-speed videography at different time scales by quantitatively characterizing the displacement of trailing edge, centroid, and leading edge (Movie S3, Supporting Information). At the moderate time scale of hundreds or dozens of milliseconds, the droplet displacements with a speed of $\approx$20 mm s^{-1} manifest a steady and increasing trend, which corresponds to the actual fact that we observe in the experiments (**Figure 2**A and Figure S4, Supporting Information). However, at the time scale of several milliseconds, the displacement shows a sinusoidal-shaped change trend in Figure S5, Supporting Information, and changes of leading contact angle and trailing contact angle as a function of time are measured to characterize the droplet motion over every groove when there occurs a local peak–valley, as shown in in Figure 2B and Movie S4, Supporting Information. The sinusoidal shape of dynamic contact angles also indicates the sinusoidal stimulation signal generated by a signal generator.

To elucidate the physical mechanism of directional droplet transport, we consider the periodically varying and isotropic inertial driving force and the anisotropic adhesive resistance force originating from the asymmetric slippery VAODR. We begin by analyzing the base of vibrational rectification, namely, mechanical horizontal vibration, which serves as the source of inertial driving force acting on the droplet. For bare ratchets, periodic back-and-forth motion occurs under the stimulation of sinusoidal stimulation signal. By choosing a fixed line (dashed black line in Figure 2A) as transformed reference frame, the periodic sinusoidal motion of ratchets substrate relative to reference line is transformed to the sinusoidal motion of reference line relative to the fixed ratchets substrate (Figure 2C). The advantage of this reference frame transformation lies on the fact that the motion of droplets and substrate on the VAODR are both transformed to the only motion of droplets on a fixed substrate, which greatly reduces the complexity of the analysis. The displacement (X) of reference line relative to the fixed substrate in transformed reference frame is: $X = X_0\sin(2\pi f t + \varphi)$, where X_0 is the amplitude of sinusoidal motion of substrate, f is the vibration frequency, t is time, and φ is the initial phase. By taking the second

derivative of X with respect to t, the accelerated speed of reference line is: $a = d^2X(t)/dt^2 = -4\pi^2 f^2 X_0 \sin(2\pi f t + \varphi)$. Then, the inertial driving force (F_{driving}) of droplet on the VAODR could be deduced as

$$F_{\text{driving}} = -ma = 4\pi^2 m f^2 X_0 \sin(2\pi f t + \varphi) \tag{1}$$

where m is the mass of droplet. By substituting the experimental parameters of $m \approx 10$ mg (10 µL), $f \approx 48$ Hz, $X_0 \approx 58.4$ µm (amplitude $\approx$ 15 Vpp), and $\varphi \approx -1.4$, the maximum inertial driving force is deduced as 53.12 µN (Figure 2D), and the inertial driving force varied sinusoidally with time. So we obtained an isotropic periodic driving force acting on the droplet on the VAODR by utilizing mechanical horizontal vibration. What we need to enable a directional droplet motion is introducing an anisotropy to rectify the periodic motion of droplet just like the half-wave rectification in the electric field.

Capillary force analysis of the liquid corners in the vicinity of the contact lines are conducted instead of surface tension analysis on three-phase contact lines because of several underlying reasons:[42–44] 1) It is easily imagined that droplets move, namely, three-phase contact lines move, only when the driving force is larger than the maximum resistance force that the solid can produce. However, this capillary force cannot be found in Young's equation: $\gamma_{\text{LV}}\cos\theta = \gamma_{\text{SV}} - \gamma_{\text{SL}}$ and it was often confused with γ_{SV} or γ_{SL}. 2) The contact line is fully a mathematical concept, which is defined as the curve where the three phases contact. So, the force analysis based on surface tension of the three-phase contact lines has severe difficulties in practical applications of experimental analysis, and what withstands the force acted by substrate is the liquid corner in the vicinity of three-phase contact lines.

Instead of utilizing three surface tensions (γ_{SV}, γ_{SL}, and γ_{LV}), capillary forces (τ_{AL} and τ_{LV} based on the liquid cohesion of a droplet, and τ_{A} based on adhesion between the droplet and the VAODR) are analyzed (bottom panels of Figure 2E and Figure S6, Supporting Information). Deeper understanding about these three capillary forces is that τ_{AL} and τ_{LV} are the components of capillary forces acted on liquid corners along the VAODR–liquid interface and the liquid–vapor interface due to the cohesion of liquid, and τ_{A} is the capillary resistance force acted on liquid corners by the VAODR. Because three-phase contact lines always move along the direction parallel to the VAODR interface, the τ_{A} is broken into tangential and normal components $\tau_{\text{A//}}$ and $\tau_{\text{A}\perp}$. It is noted that τ_{AL}, τ_{LV}, and τ_{A} are treated as tensions with a unit of force per length. There is a mechanical balance along the normal direction of liquid corner near contact lines as droplet always propagates along the interface: $\tau_{\text{A}\perp} = \tau_{\text{LV}}\cos(\theta^* - \pi/2)$ where θ^* is the intrinsic contact angle of droplet on the flat VAODR. In fact, what we care more about is the force balance parallel to the interface of VAODR which determines the actual motion of droplets: $\tau_{\text{A//}} = \tau_{\text{AL}} + \tau_{\text{LV}}\cos\theta^*$. When droplets on the VAODR are actuated by vibrational rectification, the droplets are deformed greatly which means a large change of apparent contact angles (θ). The component of driving force along the interface of the VAODR, namely, $\tau_{\text{A//}} + \tau_{\text{LV}}\cos\theta^*$, increases until it exceeds the maximum resistance force that the VAODR can provide, namely, $\tau_{\text{A//, max}}$. Then three-phase contact line starts to move.
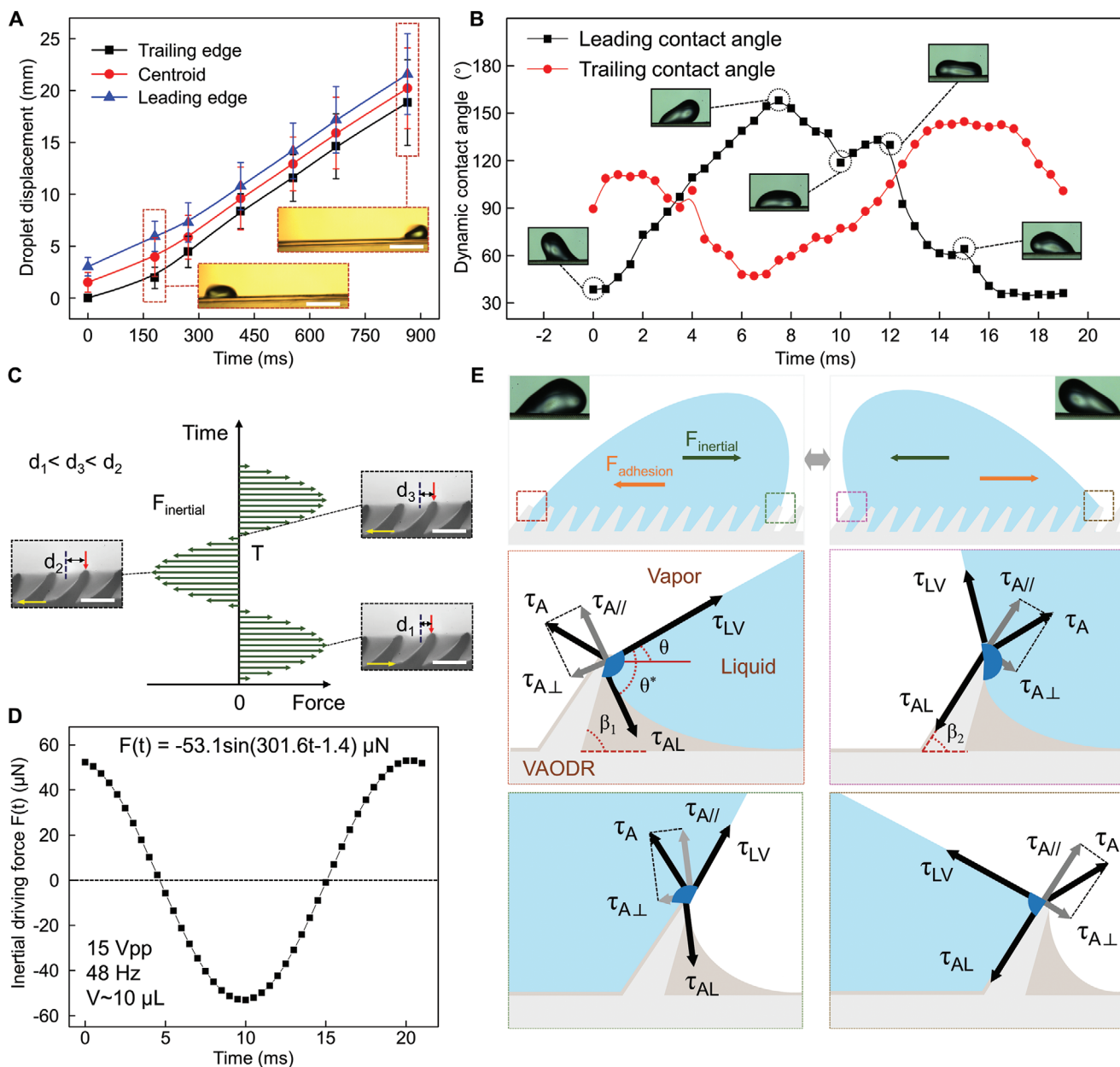
Figure 2. High-speed dynamic process and physical mechanism of directional droplet transport on the VAODR. A) The water droplet displacement of the trailing edge, centroid, and leading edge as a function of time shows a directional and rapid (≈21 mm s^{-1}) motion along the slant direction of slippery ratchets at a time scale of hundreds of milliseconds. Scale bars in insets: 2 mm. B) The dynamic apparent contact angle of a water droplet as a function of time shows the evolutions of leading and trailing contact angle. When the leading edge of the droplet climbs over a microgroove, the dynamic contact angle increases a little to show a peak–valley (black dashed circles). C) The periodically varying inertial driving force ($F_{inertial}$) originates from the isotropic periodic motion of the vibration platform relative to a reference line (black dashed line in insets). The insets show the three typical positions of vibration platform corresponding to driving forces with different amplitudes and directions. The yellow arrows indicate the direction of driving force. Scale bar in insets: 100 μm. D) The theoretical fitted line and experimentally measured data of inertial driving force of a water droplet (≈10 μL) on the VAODR actuated by horizontal vibrational rectification (vibration amplitude ≈15 Vpp, vibration frequency ≈48 Hz) within a vibration period (≈20 ms). E) Models of advancing and receding contact angles near the liquid corners show an asymmetric capillary force distribution acting on advancing and receding contact lines. When a droplet propagates along the slant direction of the slippery ratchets (red box), the slant microgrooves result in a moderate apparent contact angle (θ), which is smaller than the intrinsic contact angle (θ^*) due to the synergistic action of the three capillary forces (τ_{LV}, τ_{AL}, and τ_A) owing to the cohesion of liquid, and the adhesion of liquid and the VAODR. Mechanical analysis on the four advancing and receding contact lines (red, light-red, green, and light-green boxes) concludes an anisotropic resisting adhesion force ($F_{adhesion}$) along the opposite directions of slippery ratchets under the actuation of vibrational rectification ($F_{inertial}$), which accounts for the primary reason for droplet transport on the horizontally vibrated VAODR.

The overall adhesive resistance force difference ($\Delta F_{adhesion}$) of droplet motion on the VAODR along the two opposite directions, which can be expressed as

$$\Delta F_{adhesion} = k\gamma R[(\cos\theta_{r1} - \cos\theta_{a1}) - (\cos\theta_{r2} - \cos\theta_{a2})] \quad (2)$$

where k is a prefactor depending on the contact line shape, γ is the lubricant–liquid interface tension, R is the droplet radius along the slant direction of ratchets, θ_{ri} and θ_{ai} are the receding and advancing contact angles of a droplet on the VAODR along different directions the same as ($i = 1$) or opposite to ($i = 2$) the slant direction of ratchets.

We experimentally measure the asymmetric adhesive resistance force of droplets acted by VAODR due to the slant morphology of the anisotropic VAODR which results in an asymmetric meniscus. For instance, for a water droplet ($\approx$60 µL), the hysteresis drag force acted by the VAODR is $\approx$69 µN along the direction opposite to ratchets and $\approx$53 µN along the direction of ratchets, respectively (Figure S7, Supporting Information). This adhesive resistance force difference dominates the directional motion of droplets on the VAODR actuated by vibrational rectification.

2.3. Modulating Transport Capacity by Designing Topological Parameters of Ratchets and Tuning Vibrational Parameters of Rectification

The capacity of droplet transport including transport volume range and transport speed are precisely controlled by regulating lubricant meniscus in the ratchets and rectification originating from mechanical horizontal vibration. The meniscus of lubricant in the ratchets is regulated by both lubricant parameters such as lubricant thickness t, which has been discussed in Figure 1E, and topological parameters of ratchets, such as ratchet depth D and groove width W, and one of the all-important transport capacity, real-time modulation of droplet motion, is well-controllable by flexibly tuning the dominant vibrational parameters including frequency f and amplitude A, which is conducive to further achieving a dynamic and programmable droplet manipulation.

The lubricant meniscus in the ratchets play a key role in the interplay between the droplets and the slippery ratchets especially the shape of liquid–lubricant interface, which affects the contact area and the length of three-phase contact line corresponding to the resistance force of droplet transport applied by slippery ratchets (**Figure 3**A). The volume ranges of efficient
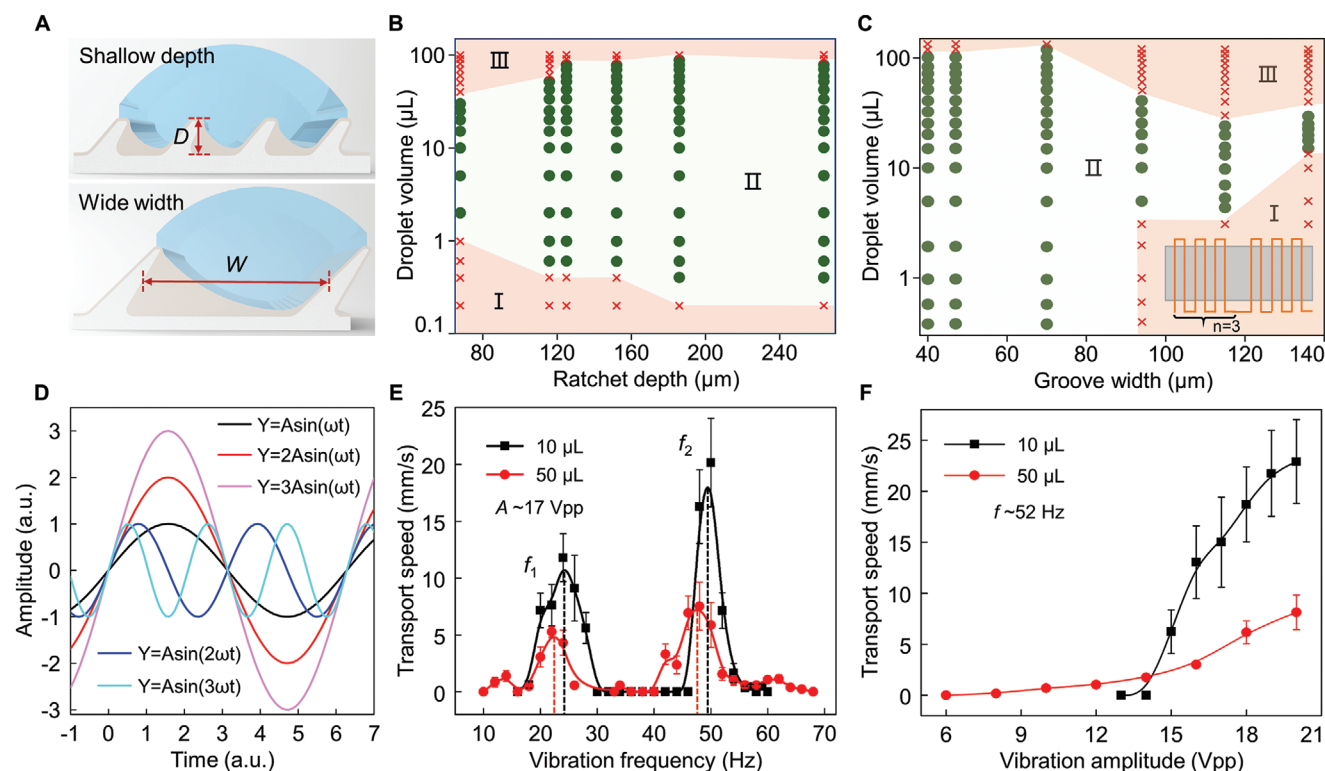

Figure 3. Modulating transport capacity of droplets including volume range and transport speed by designing topological parameters of ratchets and tuning vibrational parameters of rectification. A) Schematic illustrations of slippery ratchets with different topological parameters including shallow ratchet depth and wide groove width, which both dominate the meniscus shape of infused lubricant. B,C) Volume ranges of water droplets that can be transported on the VAODR with different ratchet depths (70–260 µm) induced by different laser power (100–350 mW) and groove widths (40–140 µm) induced by n (line-scanning replicates in a single groove, n = 1–9). Droplets on slippery ratchets with parameters located in region I and III cannot be propelled due to the inappropriate topological parameters or droplet volume, while droplets located in region II can be successfully actuated. D) Schematic demonstrating stimulation with different vibration frequencies (ω, 2ω, and 3ω) and vibration amplitudes (A, $2A$, and $3A$). E,F) Precise and controllable modulation of droplet transport velocity mediated by vibrational rectification under different frequencies (10–70 Hz) and a fixed amplitude ($A \approx$ 17 Vpp), and different amplitudes (6–20 Vpp) and a fixed frequency ($f \approx$ 52 Hz) with different droplet volumes (10 and 50 µL). There are obviously two peaks in the transport speed as a function of vibration frequency, which is possibly relevant to the system resonance due to the frequency-doubled relationship ($f_1 \approx$ 24 Hz, $f_2 \approx$ 48 Hz, $f_2 \approx f_1$).

water droplet transport can be regulated by designing and fabricating ratchets with different D and W by tuning laser power and n (line-scanning cycles in a single groove, inset of Figure 3C). Under the certain vibrational parameters ($A \approx 16$ Vpp and $f \approx 50$ Hz), there exists an optimal ratchet depth range (185–265 μm) that corresponds to a wide volume range (0.2–100 μL) of droplet transport and an optimal groove width of ≈70 μm that corresponds to a largest droplet volume of ≈120 μL. Regions I and III correspond to the absence of droplet transport, while region II corresponds to the efficient droplet transport (Figure 3B,C). Generally, the controllable volume ranges of droplet transport increases with the increase of ratchets depth due to the more anisotropy of lubricant meniscus. When the n exceeds 3, namely, W exceeds ≈93 μm, the volume range decreases greatly as a result of the less number of ratchets associated with a droplet.

To further achieve the flexible and universal manipulation of droplets by tuning the real-time droplet transport capacity, parameters relevant to vibrational rectification including frequencies (f) and amplitudes (A) are studied in detail. Schematic of stimulation signals with different amplitudes and frequencies is shown in Figure 3D. There are two peaks in the plot of transport speed of water droplets as a function of vibration frequency (Figure S8, Supporting Information) that are relevant to the resonant frequency of the VAODR. It is interesting that the two peaks are nearly frequency-doubled relationship ($f_2 \approx 48$ Hz and $f_1 \approx 24$ Hz, $f_2 \approx 2f_1$) (Figure 3E and Figure S9, Supporting Information). When the vibration amplitude A exceeds a critical value of ≈14 Vpp, the transport speed of droplets on the VAODR actuated by mechanical vibration increases with the vibration amplitude (Figure 3F).

2.4. High-Performance Manipulation of Omni-Droplets

The most exciting performances of the VAODR are the large volume range and fast velocity of omni-droplets transport. First, several kinds of liquids including a blood (typical biological fluid) and a glucose (typical medical fluid) droplet are chosen to be propelled on the VAODR at a climbing angle of ≈4° (Figure S10, Supporting Information). The transport of omni-droplets (20 wt% alcohol solution, Dulbecco's modified Eagle medium (DMEM), cell culture medium, glucose solution, blood and liquid metal; volume ≈5 μL) are also conducted to manifest the relation of displacement as a function of time. The static contact angle of these liquid droplets is measured on slippery ratchets to show the distinct wetting states (Figure S11, Supporting Information). Then, a large-volume water droplet (≈2 mL) is propelled on the VAODR actuated by vibrational rectification (vibration amplitude ≈20 Vpp, vibration frequency ≈54 Hz) in **Figure** 4A and Movie S5, Supporting Information, which has never been reported ever before utilizing mechanical vibration or even other transport strategies by an external field (electric, magnetic, light, and thermal field) in Table S1 and Figures S12 and S13, Supporting Information. The water droplet with the large volume of ≈2 mL has tended to flatten to a certain extent under the influence of gravity, which depends on its larger radius of ≈3.51 mm compared to capillary length $l_c = [\gamma/\rho g]^{1/2} \approx 2.73$ mm, where γ denotes the surface tension

of water, ρ denotes the mass density of water, and g denotes the gravitational acceleration. The relevant dimensionless numbers including the Bond number (Bo), capillary number (Ca), and Reynolds number (Re) have been utilized to manifest that the surface tension and gravitation force are dominant in the process of droplet motion. However, the viscous dissipation is negligible due to the small Ca. To quantify the extraordinary properties of the VAODR in the volume range and velocity of droplet transport, droplet transport with different volumes (0.2–2000 μL) under the actuation of vibrational rectification with different vibration amplitudes (14, 16, 18, and 20 Vpp) for water and glucose solution has been performed with a fast velocity (up to ≈60 mm s^{-1}) as shown in Figure 4B,C. Generally speaking, the larger the amplitude is, the faster the droplet velocity is. By bending the VAODR to a curve, we can obtain a curved VAODR for the transport of droplets in Figures S14–S16, Supporting Information. Moreover, by rolling the VAODR into a tube, we can manipulate a water slug (≈10 μL) in a VAODR-based tube, which is fabricated by rolling the VAODR membrane into a cylindrical shape and stuffing it into a hard circular tube (Movie S6, Supporting Information). It demonstrates potential application in the field of biomedical tubes and infusion therapy (Figure 4D). In addtion, the capacity of femtosecond laser patterning processing enabled us to fabricate distinct tracks with complex patterns such as an "S"-shaped track to guide an "S"-shaped transport of droplets (Figure S17, Supporting Information). Compared with the strategies that utilized the gradient of surface chemical wetting which is limited to a short transport distance, the VAODR can acquire an unlimited transport distance in theory. We have achieved a long distance (≈51 mm) of transport of omni-droplets including alcohol aqueous solution (20 and 40 wt%), glucose aqueous solution (5 wt%), water, and glycol (Figure S18, Supporting Information). Real-time control of the vibration conditions (frequency and amplitude) enables the programmable and dynamic control of multidroplets on the VAODR (Figure 4E). Four droplets with different volumes (10, 15, 20, and 30 μL) have been programmed to move in sequence at a high speed under difference vibration frequencies (Movie S7, Supporting Information). Furthermore, by tilting the VAODR a little to introduce a component of gravity, "cable-car"-like bidirectional/forth-and-back transport of alcohol solution droplet on the inclined VAODR has been obtained as shown in Figure 4F and Figure S19 and Movie S8 in the Supporting Information. This VAODR-based strategy is applied to almost all solid substrates due to the wide applicability of femtosecond laser processing and lubricant-infused technology such as typical metal (aluminum plate), semiconductor (silicon water), and polymer (silicone rubber) in Figure 4G and Figure S20, Supporting Information. To demonstrate the capacity of large-area and fast manufacturing of the VAODR, the strategy of template replicating has been utilized to fabricate a VAODR and omni-droplets transport has been demonstrated on the replicated VAODR in Figures S21–S24, Supporting Information. To further demonstrate the real-time control of droplet transport, droplet transport switching from "On" state to "Off" state reversibly by modulating the vibration frequency of vibrational rectification has also been demonstrated, as shown in Figure S25 and Movie S9, Supporting Information. The robustness and capacity for continuous transport are examined by
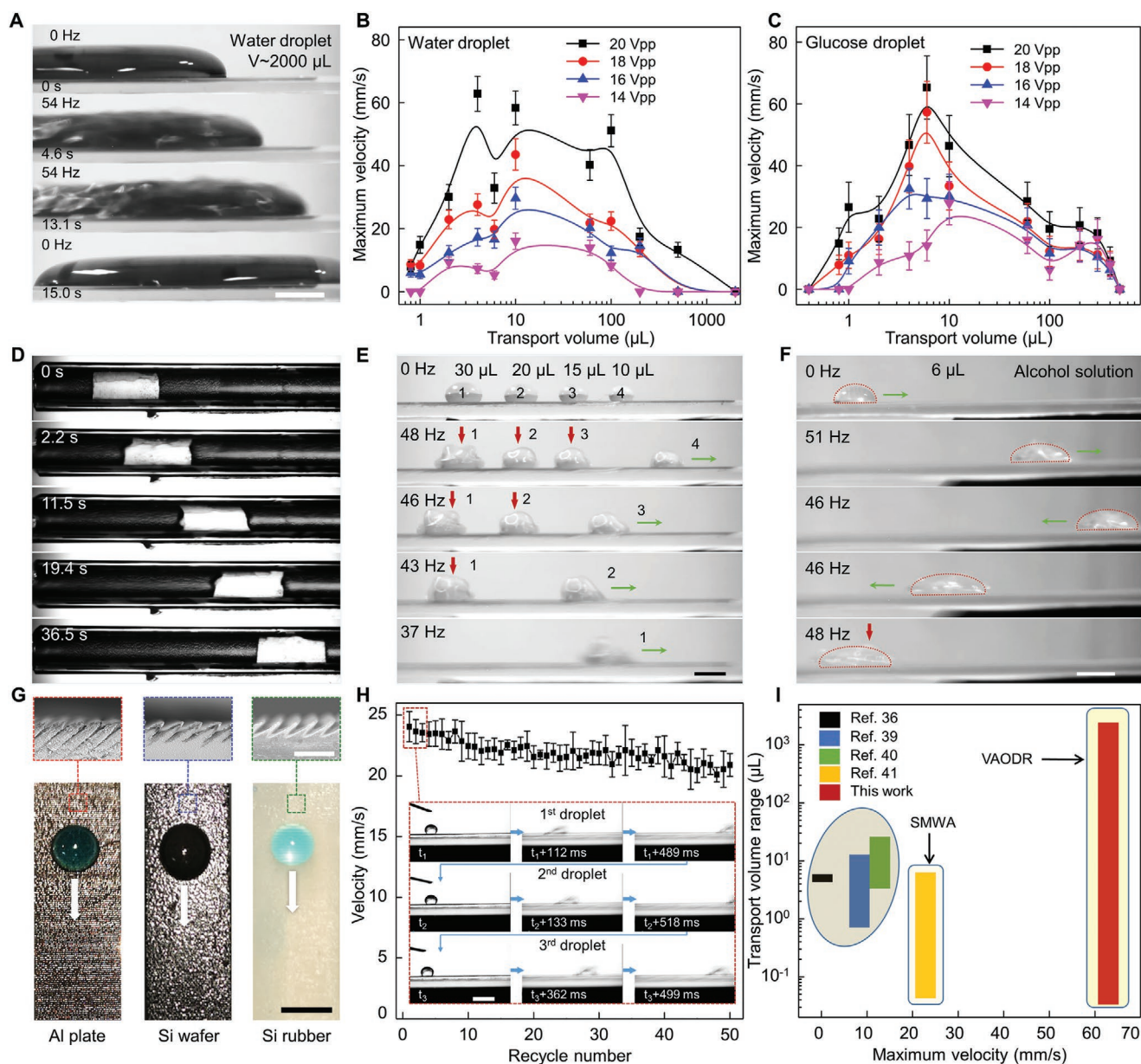
ADVANCED
SCIENCE NEWS

www.advancedsciencenews.com

ADVANCED
MATERIALS

www.advmat.de

Figure 4. High-performance (large-volume range, fast, bidirectional, and omni-substrate applicable) manipulation of omni-droplets on the VAODR. A) Selected sequential snapshots of large-volume (≈2 mL) water droplet transport on the VAODR actuated by vibrational rectification (vibration amplitude: ≈20 Vpp; vibration frequency: ≈54 Hz). The water droplet has tended to flatten under the influence of gravity, which depends on its larger radius of ≈3.51 mm compared with capillary length $l_c = [\gamma/\rho g]^{1/2} \approx 2.73$ mm where γ denotes the surface tension of water, ρ denotes the mass density of water, g denotes the gravitational acceleration. Scale bar: 1 mm. B,C) The maximum transport velocity (up to ≈60 mm s^{-1}) of water droplets and glucose solution droplets as a function of droplet volumes (0.2–2000 μL) under the stimulation of vibrational rectification with different amplitudes (14–20 Vpp) at the same frequency (≈50 Hz). The maximum transport volume and the maximum velocity both manifest the high performance of droplet manipulation especially in the maximum momentum per density (Table S1, Supporting Information). D) Transport of a water slug (≈10 μL) on VAODR-based tubes fabricated by rolling the VAODR membrane into a cylindrical shape and stuffing into a hard circular tube. Scale bar: 2 mm. E) Programmable and sequential transport of multidroplets with different volumes (10, 15, 20, and 30 μL) by the real-time and dynamic regulation of vibrational frequencies (f: 48, 46, 43, and 37 Hz). Scale bar: 1 mm. F) "Cable-car"-like transport of alcohol solution droplet (≈6 μL) for a "back-and-forth" bidirectional motion. Scale bar: 2 mm. G) Transport of droplets applies to almost all solid omni-substrates including typical metals (aluminum plate), semiconductors (silicon wafers), and polymers (silicone rubbers). Black scale bar: 3 mm. White scale bar: 200 μm. H) Continuous transport of multidroplets on the VAODR demonstrating the robustness (recycle number >50) and reproducibility (maximum velocity >20 mm s^{-1}) of vibrational rectification actuation. The insets show the selected transport snapshots of the first three droplets. Scale bar: 4 mm. I) Comparison of droplet transport performance among previous work utilizing mechanical vibration for droplet transport. The maximum velocity (>60 mm s^{-1}) in this work is above three times larger than those of previous works, and the volume range (0.05–2000 μL, $V_{max}/V_{min} \approx 40\,000$) is larger over three orders of magnitude.

dropping a water droplet on the VAODR continuously up to 50 cycles as shown in Figure 4H, and all the droplets are motivated with a high speed (>20 mm s^{-1}) in Movie S10, Supporting Information. During the process of continuous droplets transport, each droplet motion may entrain a little lubricant oil in microscales and slightly reduce the lubricant thickness, and then change the distribution of lubricant layer to a certain degree. This kind of lubricant entrainment is negligible in determining the capacity of droplet manipulation, which is verified by little decrease of droplet velocity within 50 cycles of droplets transport and the fact that there is no obvious change in the lateral profile of the lubricant meniscus. The grade ability (up to ≈7°) of droplet transport on the VAODR has been demonstrated to demonstrate the capacity of antigravity (Movie S11, Supporting Information). Finally, several classical works relevant to droplet transport by mechanical vibration are compared as displayed in Figure 4I. It is concluded that the VAODR has a great capacity in controlling droplet transport especially in volume ranges (0.05–2,000 µL, V_{max}/V_{min} ≈ 40 000) and maximum transport speed (≈60 mm s^{-1}) that is three orders of magnitude and three times higher than previous works,[36–41] respectively. In addition, liquids with different viscosities, such as glycerol–water mixture, and different surface tensions, such as alcohol–water mixture, have been chosen to be manipulated on the VAODR. The results show that viscous liquid with viscosity up to 219 mPa s and lyophilic liquid with surface tension down to 46 mN m^{-1} could both be transported.

2.5. Biomedical Detection and Drugs Screening, and the Portable Functional Devices based on VAODR

The versatile transport of omni-droplets on the VAODR mediated by vibrational rectification can be harnessed for many practical applications especially in biomedical detection. For instance, Zhao et al. have created and utilized biomedical materials with microstructures for biological sensing and bionic organ chips based on droplet manipulation.[45–47] The left panels of **Figure 5**A show the ABO blood-group test by mixing a blood sample with antibody reagent (Movie S12, Supporting Information). The time of reaction will be reduced to a certain degree due to the vibration that promoted the mixing of blood and reagents. The right panels of Figure 5A show microscopy photographs of agglutination (B-antigen and B-antibody) and no agglutination (B-antigen and A-antibody). In addition, anticancer drug screening is conducted on the VAODR by vibrational rectification due to the good biocompatibility of the VAODR (Figure S26, Supporting Information), which is performed specifically by utilizing doxorubicin hydrochloride (DOX) drugs and HeLa cells. By transporting a droplet of the DOX–PBS (phosphate buffered saline) mixture to mix with a droplet of the HeLa cells culture medium, we obtain a good effect of cell killing (left panels in Figure 5B and Figure S27, Supporting Information). The HeLa cell viability is quantitatively characterized by counting the rate of live cells as a function of time (Figure 5C and Figure S28 and Movie S13, Supporting Information). Droplets of the DOX–PBS mixture with different volumes and concentrations are manipulated by the VAODR to treat the HeLa cells for a controllable HeLa

cell mortality, which is potentially applicable in biological fields (Figure 5D and Figure S29, Supporting Information). To further demonstrate practical applications, a hand-held vibrational droplet rectification detection gun based on the VAODR is designed and fabricated as shown in Figure 5E–G. The sample reactant can be transported at a high velocity to mix with detection reagents for a controllable and fast detection in Figure 5H and Movie S14, Supporting Information. By bending the VAODR sample to a curved shape, the horizontal random motion of droplets can be effectively restrained (Movie S15, Supporting Information). Finally, we conceptually design a portable biomedical detection kit with multichannels for an integrated detection (Figure 5I–L). In addition, a VAODR with four channels is demonstrated to manipulate reactant droplets with different volumes within 11 s in a controlled and programmed manner (Figure S30 and Movie S16, Supporting Information). Due to the encapsulation of shells from the outside environment and the selectable lubricant from a series of liquids in pharmaceutical grade and food grade, there is nearly no contamination even in outside open environments. In addition to biomedical detection, other general applications including liquid droplet lenses, biocompatibility, liquid microreactions, and "cargo"-like transport of foam balls have been demonstrated to reveal the versatile performance and multifunctionalities of droplet transport on the VAODR by vibrational rectification (Figures S31–S33 and Movies S17 and S18, Supporting Information). The stability of droplets vibration could be successfully verified by regulating the droplet position in real time and dynamically in a velocity-controllable manner, which is crucial for practical applications.

3. Conclusions

We have demonstrated a powerful (fast, programmable, and robust) strategy to manipulate omni-droplets with large volume ranges in a biocompatible way by leveraging the conjunction between the slippery ratchets fabricated by femtosecond laser ablation[48–51] and mechanical vibration. The high performance of droplet transport is achieved in this platform including large volume range (0.05–2000 µL, V_{max}/V_{min} ≈ 40 000) and fast speed (≈60 mm s^{-1}), which is three orders higher and three times higher compared with previously reported approaches that utilize vibration, respectively. Moreover, the maximum transport volume (≈2 mL) is relatively large which is by far less known even under the actuation of stimulation by other external fields (Table S1, Supporting Information). The prominent improvement in droplet transport capacity can promote the development in the field of vibration-actuated droplet transport and furthermore construct a fully novel concept of a VAODR (vibration field) which is analogous to other four primary strategies utilizing external-field-induced droplet transport including electrowetting or electrodewetting (electric field), magnetic actuation (magnetic field), light irradiation (light field), heat/evaporation (heat field), and mechanical vibration. From a broader perspective, the generality of our strategy could open a new and complementary avenue for a large range of applications from biomedical detection and droplet microfluidics.
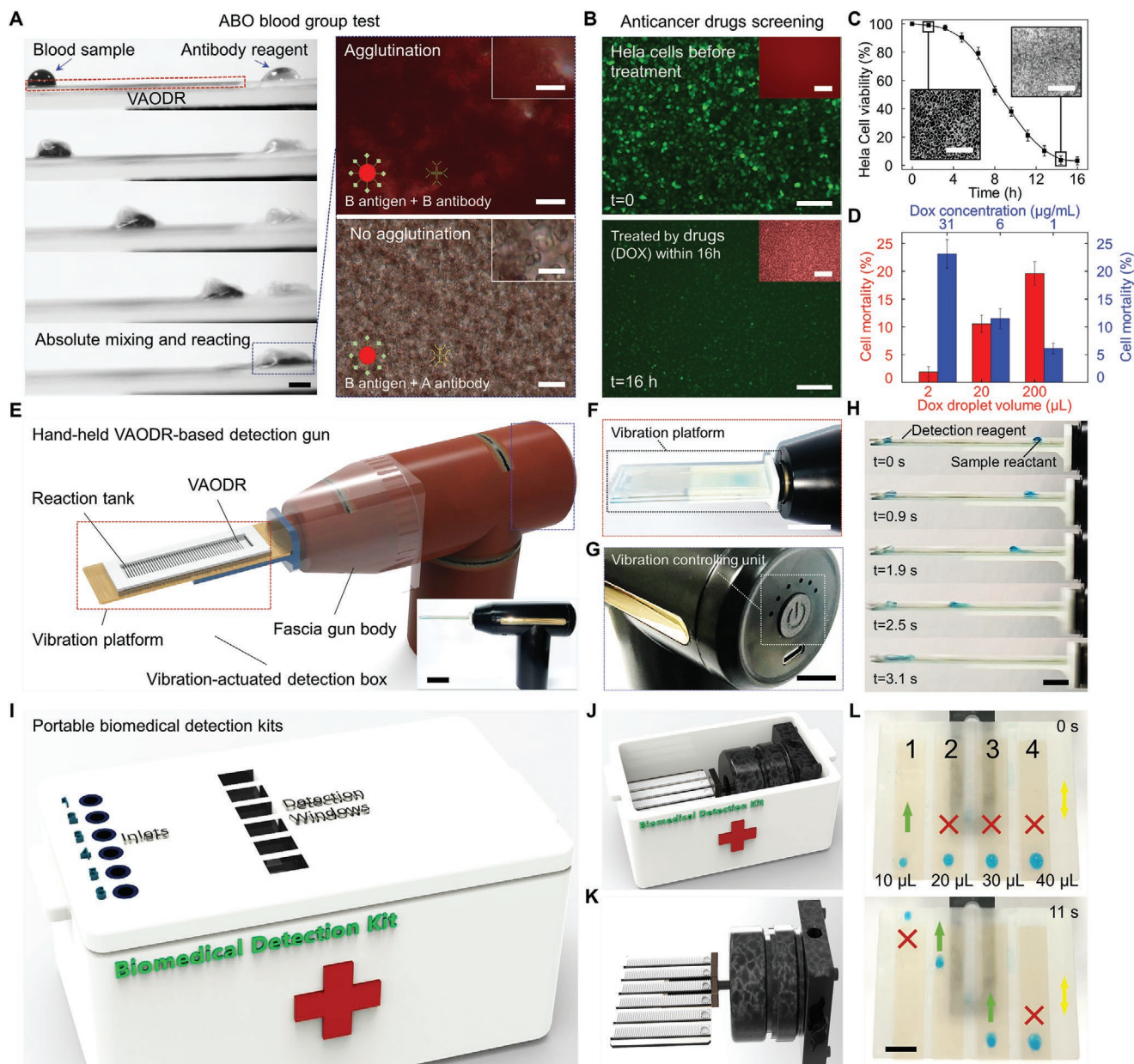
**ADVANCED
SCIENCE NEWS**

www.advancedsciencenews.com

**ADVANCED
MATERIALS**

www.advmat.de

Figure 5. Blood-group test and anticancer drug screening, and the portable biomedical detection devices based on the VAODR. A) Selected sequential snapshots showing the ABO blood-group test by mixing blood samples including antigens with antibody reagents on the VAODR. The mechanical horizontal vibration is beneficial to further reaction and reducing the reaction time. The top right panel shows the agglutination of blood sample (B-antigen) with detection reagent (B-antibody), while the bottom right panel shows no agglutination of blood (A-antigen) with detection reagent (B-antibody). The schematics in the left bottom corner of the right panels demonstrate the corresponding red blood cell types as well as antigens in red blood cells, and antibodies in plasma. Black scale bar in the left panel: 3 mm. White scale bars in right panels: 60 µm. White scale bars in right insets: 20 µm. B) Fluorescence images demonstrating the HeLa cell viability before treatment by DOX drugs at 0 h and after treatment within 16 h, which shows potential for new anticancer drug screening. The insets show the death of HeLa cells. Scale bars in panels: 100 µm. Scale bars in insets: 50 µm. C) HeLa cell viability decreases with the increase of time after drug treatment within 16 h. The insets show bright-field photographs of the HeLa cells. Scale bars: 100 µm. D) HeLa cell viability after treatment by DOX drugs with different concentrations (1, 6, and 31 µg mL^{-1}) and same droplet volume of ≈125 mL, and the different volumes (2, 20, and 200 µL) and same concentration of ≈500 µg mL^{-1}. E) Schematic illustrating the hand-held VAODR-based detection gun which consists of the fascia gun body, vibrational detection box (vibration platform, slippery ratchets, and reaction tank). The inset demonstrates the side-view profile display. Scale bar in inset: 30 µm. F) Magnified profile display of vibration platform. Scale bar: 20 µm. G) Vibration control unit of the VAODR-based detection gun. Scale bar: 10 µm. H) Mixing of sample reactant and detection reagent droplet by a hand-held VAODR-based detection gun. Scale bar: 10 mm. I) Schematic illustrating portable biomedical detection kit with multichannels which can achieve integrated detection. J,K) Schematics showing the interior structure of the detection kit and the core components (multichannels-based VAODR). L) Integrated transport of multidroplets in multichannels on four slippery ratchets packed in core component of portable biomedical detection kit. Time: 0–11 s. Scale bar: 10 mm.

4. Experimental Section

Preparation of Materials: The PDMS membrane was prepared by five steps: 1) Mixing the cross-linker and the prepolymer (Sylgard 184 Kit, Dow Corning) at a ratio of 1:12 w/w. 2) Degasification for ≈10 min. 3) Spin coating after the mixture was deposited on the glass slide placed on spin coater. The film thickness of PDMS was controlled by rotation speed (200–1000 rpm) and time (0–10 min). 4) Curing on a heating plate for 2 h at ≈65 °C to form a piece of flat and homogenous PDMS film with a fixed thickness (≈500 μm). 5) The film was cut into several pieces with different sizes (length: 30 and 60 mm; width: 8 and 20 mm) for the fabrication of the vibrational omni-droplet rectifier (VAODR) by FLOA. The aluminum plates (purity: ≈99.5%, thickness: 500 μm) were purchased from New Metal Material Tech. Co., Ltd., Beijing, China. The silicon wafer (purity: ≈99.9%, thickness: 500 μm) was purchased from Taobao. The silicone rubber (purity: ≈99.0%, thickness: 1 mm) was purchased from a supermarket. Alcohol aqueous solution (20 wt%) was fabricated by mixing the absolute alcohol (C_2H_5OH, purity: >99%, density: 0.798 g cm^{-3}) and deionized water (H_2O, density: 1 g cm^{-3}). DMEM cell culture medium was purchased from ThermoFisher Co., Ltd., China. Glucose aqueous solution was fabricated by dissolving glucose powder with deionized water. The blood sample was obtained from The First Affiliated Hospital of USTC. The EGaIn (75 wt% Ga, 25 wt% In) liquid metal was exploited. The lubricant silicone oil was used for the preparation of the VAODR. The HeLa cells were purchased from the Hunan Feng Hui biological company in China. The DOX drug was purchased from the Yuanye Biological Company in China. These experiments were not subject to ethical approval, and the blood samples were not taken specifically for these experiments.

Preparation of VAODR: Diverse substrates including PDMS films, aluminum plates, silicon wafers, and silicone rubbers were first cleaned ultrasonically with deionized water for 10 min. Then, an oblique femtosecond laser (pulse width: 100 fs; repetition rate: 1 kHz; central wavelength: 800 nm) from a one-box regenerative amplified Ti:sapphire femtosecond laser system (Solstice Ace, Spectra-Physics, USA) was focused by a lens ($f ≈ 30$ mm) on the substrates deposited on a high-speed motion stage which could scan along the X/Y coordinate directions, which served as a line-by-line scanning strategy. The scanning space between two adjacent lines could be finely modulated. The laser power ranged from 20 to 500 mW, and the scanning speed ranged from 1 to 10 mm s^{-1}. The lubricant silicone oil was then infused to the anisotropic ratchets fabricated FLOA to form a slippery ratchet, namely, the VAODR. The oil film thickness was controlled by spin coating speed and time.

Instrument and Characterization: SEM images were utilized to analyze the surface topography of the laser-induced PDMS film via use of a field-emission scanning electron microscope (JSM-6700F, JEOL, Japan). The contact angles of the water were measured on the slant microwalls surface with a contact angle system (CA100D, Innuo, China). The volume of the water droplet was set to be 5 μL. The average values were obtained by measuring five droplets at different locations on the same PDMS film. All the contact and rolling angle measurements were conducted under 10% humidity and 20 °C temperature, respectively.

Droplet Transport on VAODR by Vibrational Rectification: Powerful mechanical vibrations as the source of vibrational rectification were generated to actuate the VAODR platforms via the use of a vibration generator (2185.00, Frederiksen, Australia). The stimulation signal was sent from a signal generator (DG 5000, RIGOL, China).

Supporting Information

Supporting Information is available from the Wiley Online Library or from the author.

Conflict of Interest

The authors declare no conflict of interest.

Author Contributions

Y.Z. and D.W. conceived the research and designed the experiments. D.W. and Z.W. supervised the research. Y.Z., L.X., J.W., T.W., Y.J., S.J., C.L., S.F., J.Z. carried out the experiments. Y.P., B.L., C.C., S.Z. built the analytical models. All authors analyzed and interpreted the data and wrote the paper.

Data Availability Statement

The data that support the findings of this study are available from the corresponding author upon reasonable request.

[1] G. Huang, M. Li, Q. Yang, Y. Li, H. Liu, H. Yang, F. Xu, *ACS Appl. Mater. Interfaces* **2017**, *9*, 1155.

[2] C. J. Huang, W. F. Fang, M. S. Ke, H. Y. E. Chou, J. T. Yang, *Lab Chip* **2014**, *14*, 2057.

[3] Y. Zhang, S. Park, K. Liu, J. Tsuan, S. Yang, T. H. Wang, *Lab Chip* **2011**, *11*, 398.

[4] M. Washizu, *IEEE Trans. Ind. Appl.* **1998**, *34*, 732.

[5] W. H. Tan, S. Takeuchi, *Lab Chip* **2006**, *6*, 757.

[6] L. Frenz, A. El Harrak, M. Pauly, S. Bégin-Colin, A. D. Griffiths, J. C. Baret, *Angew. Chem., Int. Ed.* **2008**, *47*, 6817.

[7] C. G. Yang, Z. R. Xu, J. H. Wang, *TrAC, Trends Anal. Chem.* **2010**, *29*, 141.

[8] R. Seemann, M. Brinkmann, T. Pfohl, S. Herminghaus, *Rep. Prog. Phys.* **2011**, *75*, 016601.

[9] K. Zhang, Q. Liang, X. Ai, P. Hu, Y. Wang, G. Luo, *Lab Chip* **2011**, *11*, 1271.

[10] M. Zhang, X. Gong, W. Wen, *Electrophoresis* **2009**, *30*, 3116.

[11] M. K. Chaudhury, G. M. Whitesides, *Science* **1992**, *256*, 1539.

[12] H. Chen, T. Ran, Y. Gan, J. Zhou, Y. Zhang, L. Zhang, L. Jiang, *Nat. Mater.* **2018**, *17*, 935.

[13] J. Li, X. Zhou, J. Li, L. Che, J. Yao, G. McHale, Z. Wang, *Sci. Adv.* **2017**, *3*, eaao3530.

[14] H. Chen, P. Zhang, L. Zhang, H. Liu, Y. Jiang, D. Zhang, L. Jiang, *Nature* **2016**, *532*, 85.

[15] M. Prakash, D. Quéré, J. W. Bush, *Science* **2008**, *320*, 931.

**ADVANCED
SCIENCE NEWS**

www.advancedsciencenews.com

**ADVANCED
MATERIALS**

www.advmat.de

[16] Y. Zheng, H. Bai, Z. Huang, X. Tian, F. Q. Nie, Y. Zhao, J. Zhai, L. Jiang, *Nature* **2010**, *463*, 640.

[17] E. Lorenceau, D. Quere, *J. Fluid Mech.* **2004**, *510*, 29.

[18] K. Li, J. Ju, Z. Xue, J. Ma, L. Feng, S. Gao, L. Jiang, *Nat. Commun.* **2013**, *4*, 2276.

[19] C. Li, H. Dai, C. Gao, T. Wang, Z. Dong, L. Jiang, *Proc. Natl. Acad. Sci. USA* **2019**, *116*, 12704.

[20] W. Kim, F. Peaudecerf, M. W. Baldwin, J. W. Bush, *Proc. R. Soc. B* **2012**, *279*, 4990.

[21] J. Li, N. S. Ha, R. M. van Dam, *Nature* **2019**, *572*, 507.

[22] A. R. Wheeler, *Science* **2008**, *322*, 539.

[23] J. Nie, Z. Ren, J. Shao, C. Deng, L. Xu, X. Chen, Z. L. Wang, *ACS Nano* **2018**, *12*, 1491.

[24] Q. Sun, D. Wang, Y. Li, J. Zhang, S. Ye, J. Cui, X. Deng, *Nat. Mater.* **2019**, *18*, 936.

[25] X. Liu, N. Kent, A. Ceballos, R. Streubel, Y. Jiang, Y. Chai, T. P. Russell, *Science* **2019**, *365*, 264.

[26] W. Wang, J. V. Timonen, A. Carlson, D. M. Drotlef, C. T. Zhang, S. Kolle, J. Aizenberg, *Nature* **2018**, *559*, 77.

[27] W. Lei, G. Hou, M. Liu, Q. Rong, Y. Xu, Y. Tian, L. Jiang, *Sci. Adv.* **2018**, *4*, eaau8767.

[28] J. V. Timonen, M. Latikka, L. Leibler, R. H. Ras, O. Ikkala, *Science* **2013**, *341*, 253.

[29] J. Wang, W. Gao, H. Zhang, M. Zou, Y. Chen, Y. Zhao, *Sci. Adv.* **2018**, *4*, eaat7392.

[30] J. A. Lv, Y. Liu, J. Wei, E. Chen, L. Qin, Y. Yu, *Nature* **2016**, *537*, 179.

[31] D. Psaltis, S. R. Quake, C. Yang, *Nature* **2006**, *442*, 381.

[32] A. Bouillant, T. Mouterde, P. Bourrianne, A. Lagarde, C. Clanet, D. Quéré, *Nat. Phys.* **2018**, *14*, 1188.

[33] J. Li, Y. Hou, Y. Liu, C. Hao, M. Li, M. K. Chaudhury, Z. Wang, *Nat. Phys.* **2016**, *12*, 606.

[34] N. J. Cira, A. Benusiglio, M. Prakash, *Nature* **2015**, *519*, 446.

[35] G. Lagubeau, M. L. Merrer, C. Clanet, D. Quéré, *Nat. Phys.* **2011**, *7*, 395.

[36] S. Daniel, M. K. Chaudhury, *Langmuir* **2002**, *18*, 3404.

[37] S. Daniel, S. Sircar, J. Gliem, M. K. Chaudhury, *Langmuir* **2004**, *20*, 4085.

[38] S. Daniel, M. K. Chaudhury, P. G. De Gennes, *Langmuir* **2005**, *21*, 4240.

[39] N. A. Malvadkar, M. J. Hancock, K. Sekeroglu, W. J. Dressick, M. C. Demirel, *Nat. Mater.* **2010**, *9*, 1023.

[40] T. A. Duncombe, E. Y. Erdem, A. Shastry, R. Baskaran, K. F. Böhringer, *Adv. Mater.* **2012**, *24*, 1545.

[41] D. Wu, Z. Zhang, Y. Zhang, Y. Jiao, S. Jiang, H. Wu, L. Jiang, *Adv. Mater.* **2020**, *32*, 2005039.

[42] J. Fan, J. De Coninck, H. Wu, F. Wang, *Phys. Rev. Lett.* **2020**, *124*, 125502.

[43] A. Marchand, J. H. Weijs, J. H. Snoeijer, B. Andreotti, *Am. J. Phys.* **2011**, *79*, 999.

[44] M. V. Berry, *Phys. Educ.* **1971**, *6*, 79.

[45] L. Sun, F. K. Bian, Y. Wang, X. Zhang, Y. Zhao, *Proc. Natl. Acad. Sci. USA* **2020**, *117*, 4527.

[46] H. Zhang, G. Chen, G. Yu, J. Guo, Q. Tan, Y. Zhao, *Adv. Sci.* **2020**, *7*, 2000789.

[47] X. Zhang, L. Sun, Y. Yu, F. Bian, Y. Wang, Y. Zhao, *Proc. Natl. Acad. Sci. USA* **2019**, *116*, 20863.

[48] L. Jiang, A. D. Wang, B. Li, T. H. Cui, Y. F. Lu, *Light: Adv. Manuf.* **2018**, *7*, 17134.

[49] S. A. Jalil, B. Lai, M. ElKabbash, J. Zhang, E. M. Garcell, S. Singh, C. Guo, *Light: Adv. Manuf.* **2020**, *9*, 122.

[50] C. Pan, L. Jiang, J. Sun, Q. Wang, F. Wang, K. Wang, Y. Lu, Y. Lu, L. Qu, T. Cui, *Light: Adv. Manuf.* **2020**, *9*, 775.

[51] Y. Xiao, R. Ming, M. Lai, X. Li, Y. Ma, X. Ming, *Adv. Photonics* **2021**, *58*, 1714001.